Why this location

Shoreham port was selected as a demonstration site as a port facility in an estuarine environment with known corrosion issues. It has also been a site of an ongoing collaboration between the Port Authority and the University of Brighton investigating mechanisms and environmental controls on microbially influenced corrosion and accelerated low water corrosion. As such it had existing monitoring infrastructure at the start of the project, and historical monitoring data that could be used to inform planning, experimental design and the early stages of algorithm development on the SOCORRO project.

Baseline/starting situation

Shoreham Port, is an active commercial port facility situated at the mouth of the River Adur in West Sussex, UK. The harbour bed sediment is dominantly of silt grade quartz and calcite, with kaolinite and illite clays and a significant organic content. Historically the port also hosted a coal fired power station, and harbour sediments have significant organic carbon content. All berthing areas within the port are constructed in an identical fashion: vertically driven carbon steel piling form the quay face, capped in concrete, with levelled rubble infill and tarmac top layer behind.

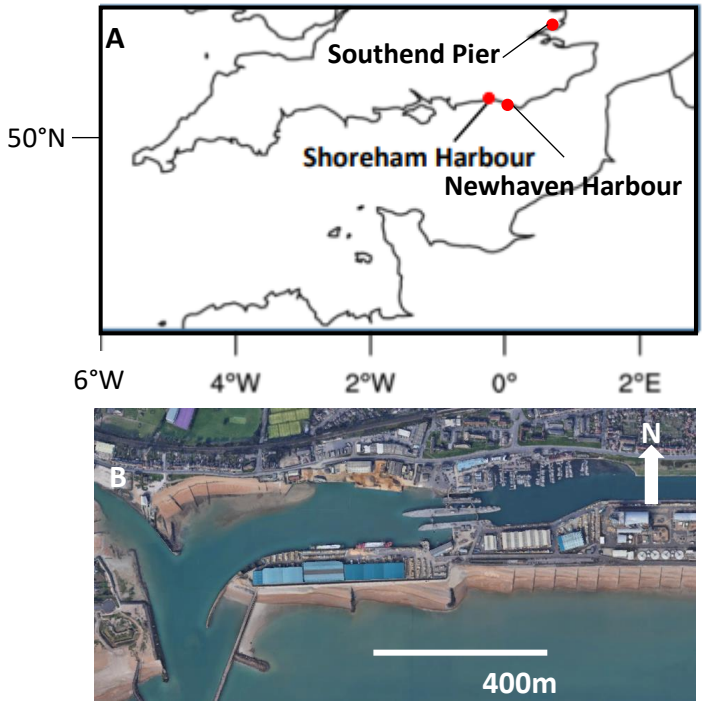

Figure SH1: Location and Google Earth Image of Shoreham Harbour.

Estimates of the tidal and non-tidal areas perimeter indicate the presence of approximately 6 km of steel piling. The piling is a mixture of both U-profile and Z-profile types. The age of piling installed prior to 2005 is not known, but where records exist, some sections of the piling wall can be dated back to the early 20th century. Areas of corrosion consistent with the physical appearance of MIC were initially noted prior to 2011. MIC-like corrosion has been observed in all three principle areas under port jurisdiction (Rousell 2012). The sampling location lies within the tidal section of the port, adjacent to the main locks, known as the Dredger Berth (50°49'46"N; 0°14'20"W). Access to the piling face and sediment bed was via a permanently moored floating jetty. Additional access and support from the Port Authority was provided via the inshore pilot boat for access and safety during installations.

The Shoreham site had a program of baseline environmental sampling from November 2020 to July 2021. The sampling included corrosion, water and sediment cores used for solid sediment analyses, and pore water analyses. Sub-samples of each sample type were taken for microbial analyses as these sites are subject to microbiologically

Figure SH2: Images of Shoreham Harbour environment and corrosion. (A) Study site at the Dredger Berth, surrounded by steel pile wall. (B) Corrosion sampling from floating pontoon. (C) Water sampling from floating pontoon. (D) Site of sediment core retrival.

influenced corrosion (Accelerated Low Water Corrosion). Samples were collected from intertidal sites within the port Dredger Berth. This site has a floating mooring pontoon which allowed access to bed sediment at low tide, and corrosion sampling from he steel pile wall at all states of the tide. Additional water samples were collected from within the main port basin area, which is isolated from tidal influence by a system of lock gates. Images of steel corrosion, the sampling procedure and corrosion are given in Figure SH2.

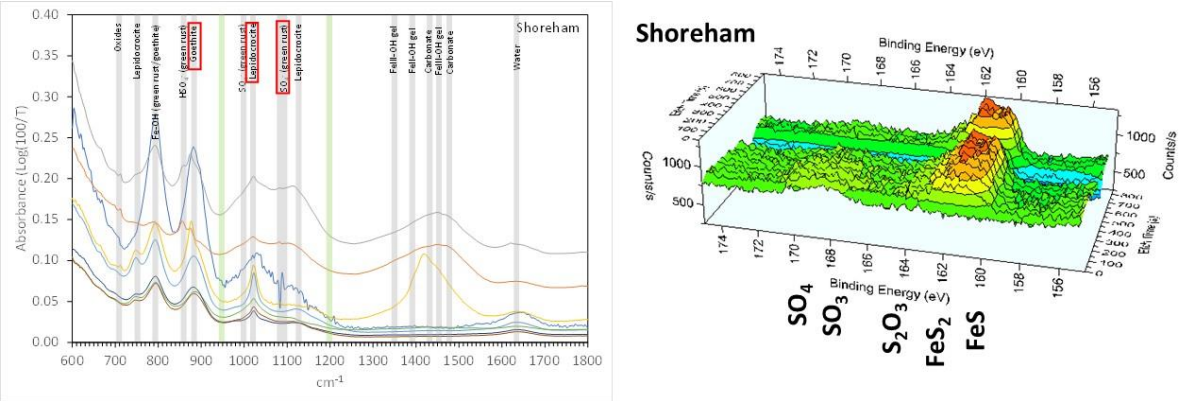

Figure SH3: Results of corrosion characteristion, Shoreham Port. (A) Fourier transform infrared spectra of corrosion products. In this case dominated by iron oxides and oxy-hydroxides alongside sulphate. (b) X-ray photoelectron spectrum of intertidal corrosion products. Sulphides and sulphate are detectable in corrosion products.

The results of mineralogical and chemical analysis of corrosion samples are shown in Figure NH3. The FTIR spectra are characterised by a broad adsorption peak from 3000-3500cm^{-1} that can be attributed to O-H groups and H_20, and multiple complex peaks in the range 600-1800cm^{-1}. Analysis of FTIR spectra was concentrated in the latter range as these absorption bands can be related to corrosion products on the steel surface. Two areas of the spectra were interpreted in detail using the PeakFit 4.12 software to deconvolute composite absorption peaks. Peaks were identified using gaussian amplitude deconvolution with a second derivative-based background fit, in separate windows from 750-1200cm^{-1} and from 1250-1750cm^{-1}. Deconvolution used a fixed full width at half maximum peak height of 18.1cm^{-1}, except for visibly narrower peaks at 861cm^{-1} and 874cm^{-1} where FWHM was reduced to fit the visible peaks. Within the intertidal corrosion samples lepidocrocite absorbance peaks at 746cm^{-1} and 1023cm^{-1} were developed in all samples (RRUFF database, Figure S2). Within samples SHDP2 absorption peaks at 781cm^{-1}, 841cm^{-1}, and 874cm^{-1}, can be attributed to Fe-OH stretching modes in sulphate green rust (Peulon et al., 2003). Peaks at 992cm^{-1}, 1095cm^{-1}, 1109cm^{-1}, and 1156cm^{-1} can be attributed to various SO_4^{2-} vibration modes in green rust ((Borda et al., 2004; Peulon et al., 2003; Rouchon et al., 2012), and that at 874cm^{-1} may also be influenced by HSO_4^- (Usher et al., 2005). The broad adsorption band from 1250-1550cm^{-1}, can be deconvoluted to peaks from ferric and ferrous hydroxide gel at 1339cm^{-1} and 1396cm^{-1} (Chernyshova, 2003), those at

1435cm^{-1} and 1473cm^{-1} to the presence of carbonate from calcite or aragonite shell material (RRUFF database), and that at 1519cm^{-1} to the O-H bond deformation. The peak at 1627-1637cm^{-1} can be attributed to water (Shahabi-Navid et al., 2020). It should be noted that the presence of biofilms in intertidal samples means that spectra may be influenced by the presence of polysaccharide biofilms on the surface (Beech et al., 2005; Zinkevich et al., 1996). We have tested for this using the spectra of reagent grade alginic acid and sodium alginate (both components of marine biofilm extra cellular polymeric substances (EPS) (Beech and Sunner, 2004; Sachan and Singh, 2020). These have characteristic absorption bands at 1244cm^{-1} and 1598cm^{-1} respectively (Figure S2) which are absent from the samples. The sulphate adsorption bands arise from the formation of sulphate green rust by sulphide oxidation as part of the MIC mechanism and could be used as a rapid diagnostic tool of accelerated microbially influenced corrosion types.

Infrared spectroscopy was been supplemented by X-ray photoelectron spectroscopy on selected samples to confirm the detailed corrosion mechanism. This technique is not suited for rapid diagnosis of corrosion type and hazard due to complexity and cost, but provides detailed information on the chemistry of corrosion products which can be used to confirm interpretations of corrosion mechanism from other techniques. This gives a firm basis for the utilisation of rapid low cost mineralogical techniques in the analysis of corrosion type. This is particularly useful for instances of microbially influenced corrosion which may lead to high corrosion rates with significant hazard to infrastructure. At Shoreham the red outer surface of the corrosion blister had a lower Fe content (~5 atom %) compared to the interior (8-11 atom%), whilst the black interior had ~6-7 atom % Fe. The reduced Fe content can be related to the presence of biofilm and calcium carbonate shell material on the outer surface. Sulphur is typically 1-2% of the bulk corrosion composition. In both red and black corrosion the outer portions of corrosion blisters are dominated by sulphate and sulphite(Figure SH3) whilst for the interiors sulphur species are dominated by iron monosulphide (amorphous or mackinawite) and iron bisulphide (amorphous or pyrite). Both $FeSO_4$ and $Fe_2(SO_4)_3$ are apparent in Fe 2p3/2 binding energy spectra for the exterior of blisters whilst FeS and FeS_2 become apparent after 840secs of sputtering. In black areas FeS_2 is the dominant sulphur species on the blister interiors. The iron sulphur compounds are accompanied by magnetite, and hematite in all cases. This confirms the accelerated low water corrosion mechanism as the production of hydrogen sulphide at the steel surface by sulphate reducing bacteria. This reacts with iron to produce iron sulphides. These are then oxidised by iron oxidising and sulphur oxidising bacteria, ultimately producing sulphate compounds. Acidity is generated at every stage, account for the highly corrosive microenvironment. A strong conclusion form this is that sulphur compounds detectable by simple spectroscopic techniques can be used as diagnostic of microbially influenced corrosion, which can then inform the SOCORRO corrosion risk assessment methodology.

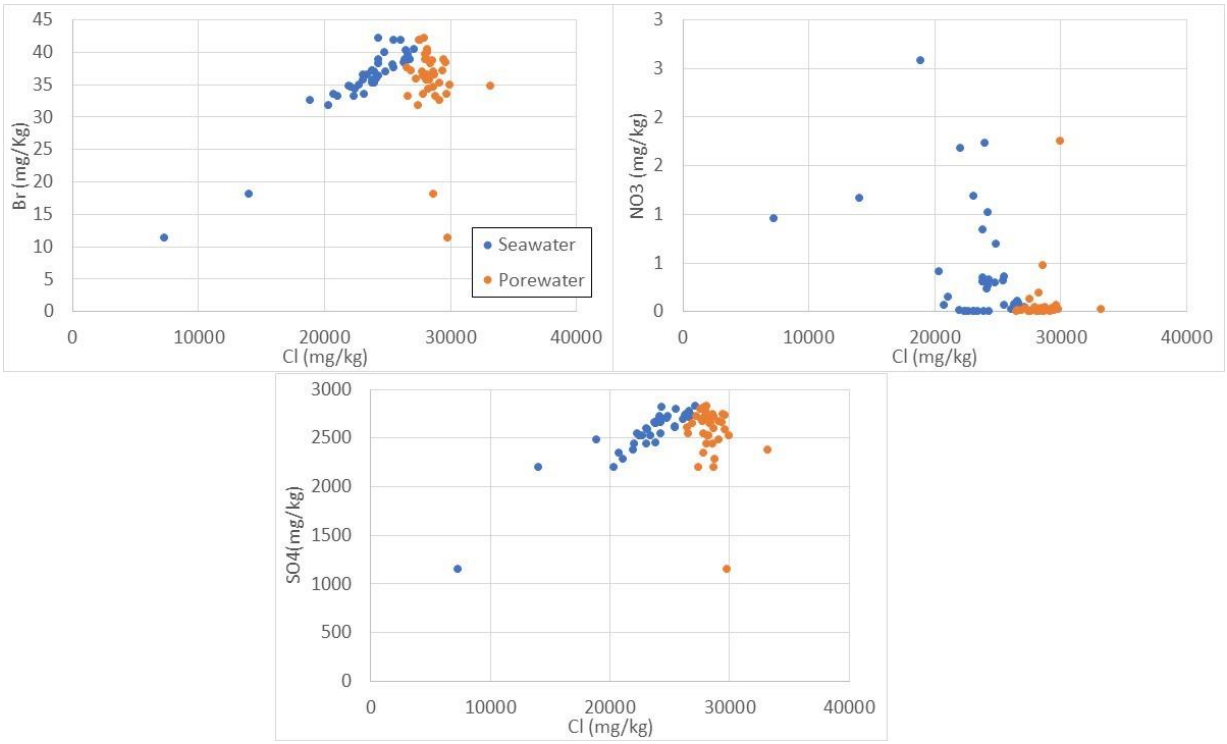

Figure SH4: Anion chemistry of sea/estuarine water and sediment porewater from Shoreham.

The environment surrounding the marine steel work was monitored in order to inform the subsequent continuous monitoring program, and to identify risk factors for microbially influenced corrosion. The anion chemistry of seawater is shown in Figures SH4 and SH5. The bromide and chloride concentrations are strongly correlated in seawater but not in sediment porewater. This is consistent with fully marine water diluted by river water in the port water column. This is typical of estuarine systems. The sediment pore waters are shifted to higher chloride concentrations than expected from un—modified seawater. This may be related to an additional chloride source from historic contamination within the sediments. Nitrate is most strongly concentrated in low salinity water. Nitrate is a nutrient contaminant, and has been previously implicated in the generation of ALWC/MIC through encouraging biofilm growth. The negative correlation with chloride concentration indicates that the main nutrient input is from river water in the estuarine system. Sulphate correlates strongly with chloride in seawater, and this reflects the same trend of seawater dilution by river water. However, sediment porewaters depart from this trend, although not as strongly as at Newhaven, extending to low sulphate concentrations. This indicates the action of sulphate reducing bacteria in the sediment, confirming anoxic bed sediment as a reservoir of causative bacteria for MIC, and identifying an environmental risk factor for accelerated corrosion types that can be used in hazard assessment.

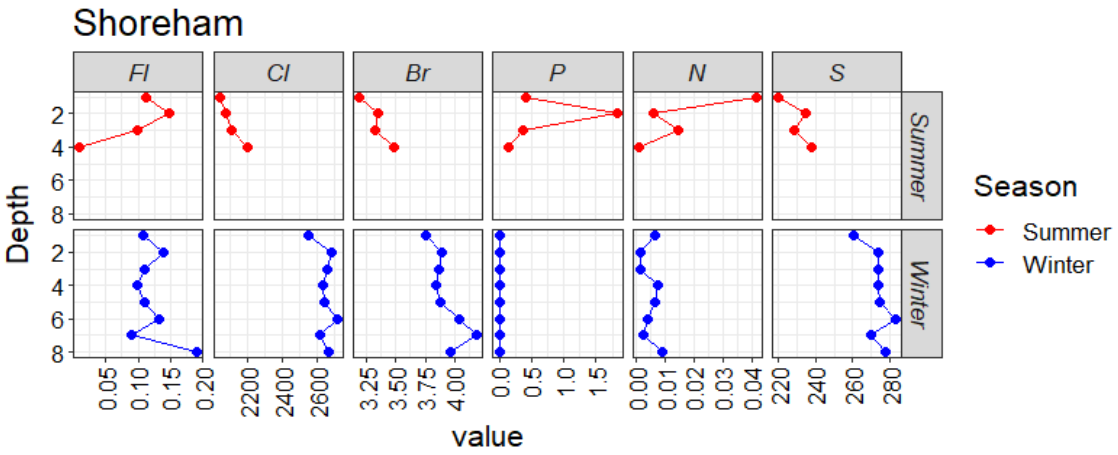

Figure SH5: Depth profiles in water column for anion chemistry.

Figure SH5 shows summer and winter season depth profiles for the port water column anion concentration. All anions reflect the estuarine environment – low concentration river water occurs on top of saline marine water due to its lower density. The exception to this is nitrate during the summer period, where lower rain fall means higher nitrate concentrations in onshore run off because of lower dilution by rainfall. There is strong seasonality in nutrient inputs to the port environment which may influence biological activity.

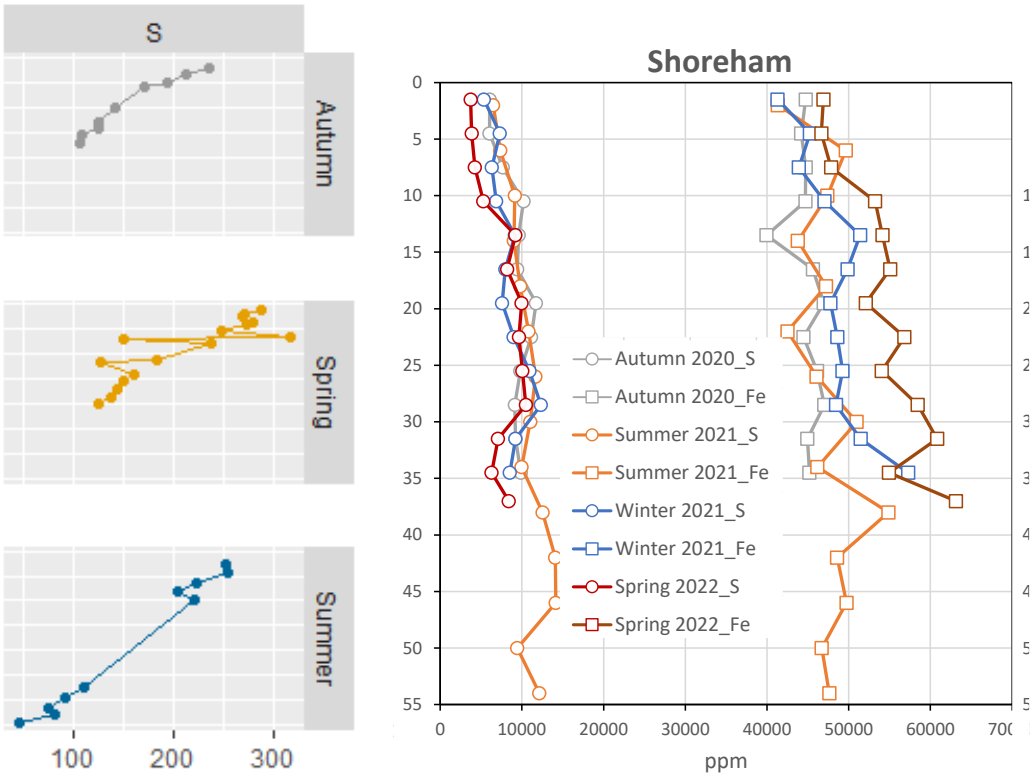

Figure SH6: Depth profiles of pore fluid (left), and solid phase iron and sulphur content (right) from sediment cores at Shoreham.

Analysis of sediment cores included solid phase iron and sulphur, and porewater iron and sulphur, sampled over 4 seasons. During all seasons the sulphate content in pore water declines rapidly with depth and the solid phase iron and sulphur increase (Figure SH6). Taken together with the pore water chemistry these are an indicator of the action of sulphate reducing bacteria in the bed sediment, using sulphate from pore water and generating iron sulphide minerals, and support bed sediment anoxia as a potential risk factor for MIC.

Selected water, sediment and corrosion samples were used for microbial metagenetic analysis at all three UK sites. They are detailed together here as comparison between sites facilitates significant findings for the SOCORRO project. Analysis of microbial abundance and diversity indices based on 16sRNA data indicates marked differences in microbial communities between the sites, whereas at each site, deep sediment and corrosion inhabitants have similar profiles. Homology results of Amplicon sequence variants (ASVs) generated by Illumina sequencing indicated Proteobacteria phylum as the dominant group, comprising 40.4% of the total ASVs, followed by Campilobacterota with 11.3% and Desulfobacterota and Firmicutes constituting about 4-5% with higher proportions in deep sediment samples. Analyses at lower taxonomic levels suggested

the presence of representatives described as corrosion causing bacteria, such as *Shewanella* sp., *Colwellia* sp., and *Mariprofundus* sp. (Figure SH7). The amplicon analysis and Fourier-transform infrared spectroscopy (FTIR) analysis of corrosion blisters show major difference at Southend-on-Sea where samples were taken in the splash zone (as intertidal samples did not return enough DNA for analysis) and from subaerial corrosion in terms of microbial population as well as corrosion products. Here typical MIC products such as sulfate green rust and intermediate oxidation state sulphur compounds are absent. Statistical analysis of the 16sRNA data (Figure SH8) indicates that at all sites the intertidal corrosion microbial communities are most similar between sediment from 50cm below surface and corrosion.

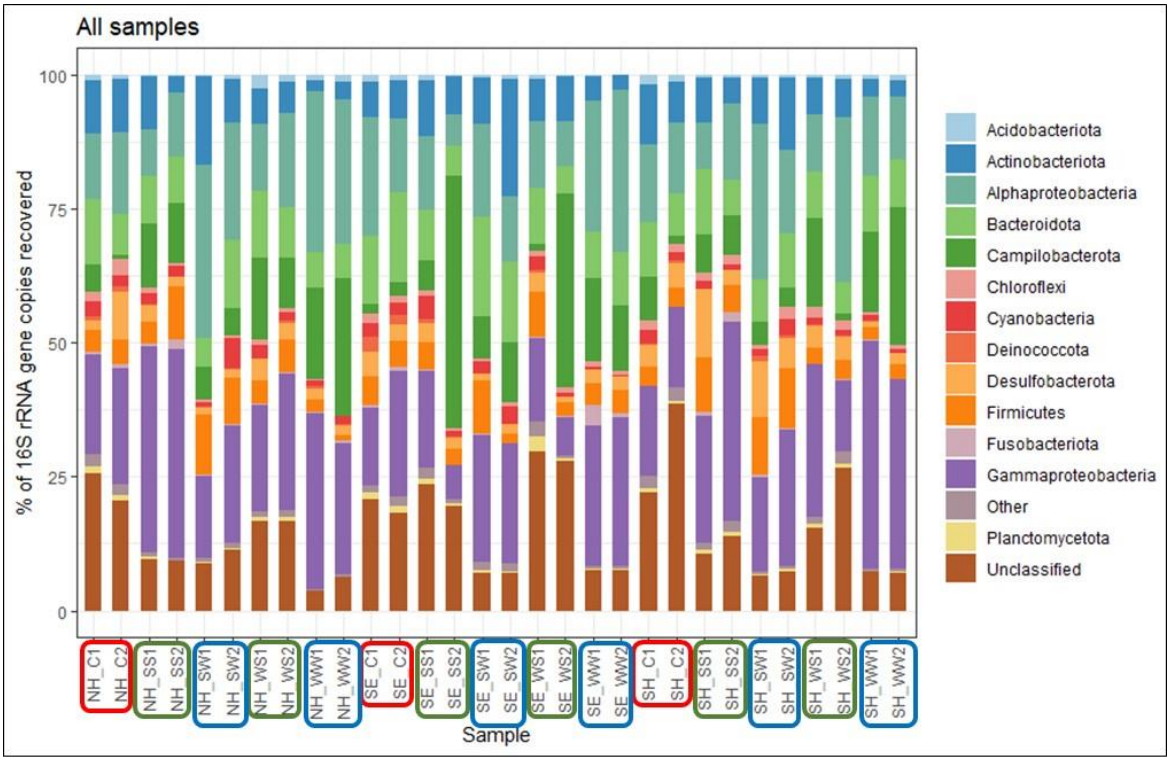

Figure SH7: Results of 16sRNA amplicon analysis of microbial sample from all UK sites.

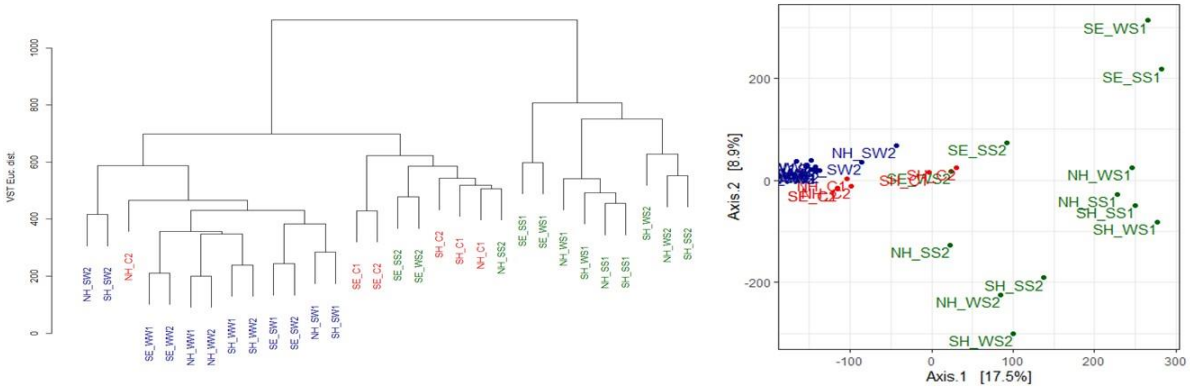

Figure SH8: Statistical analysis of 16sRNA results from all UK sites. (a) Hierarchical cluster analysis – clearly shows corrosion microbial populations are intermediate between sediment populations and seawater populations. (b) Principle components analysis – again, corrosion microbial populations are intermediate between sediment populations and seawater populations.

The corrosion associated bacterial communities are intermediate in composition between seawater and sediment. The microbial communities present in Shoreham and Newhaven corrosion include sulphate reducing, and sulphur and iron oxidising bacteria corresponding to species found in the bed sediment. This confirms the model of microbially influenced corrosion of the ALWC type resulting from the colonisation of anoxic microenvironments on the steel surface (possibly arising from the formation of biofilms) by microbial communities derive from anoxic bed sediment. Combined the with analysis of sediment chemistry this provides diagnostic criteria for hazard factors in accelerated corrosion types that can be used in corrosion risk assessment.

In order to allow diagnosis of corrosion causing microbial populations without the time and expense of a full genetic analysis we have developed a rapid identification method for S- reducing bacteria using high-resolution melt curve (HRM) analysis of the *dsr* AB gene which will enable the identification of bacteria possessing different variants of this gene.

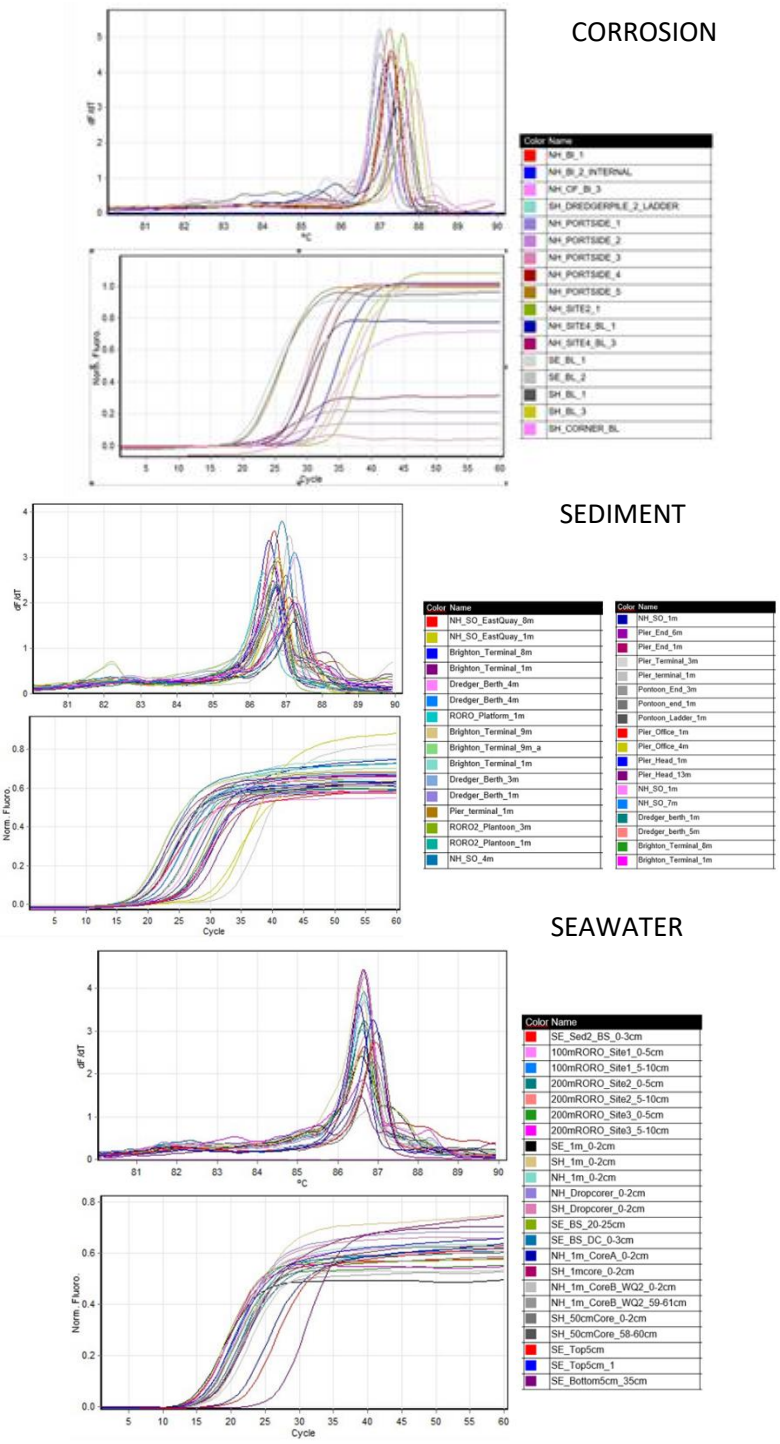

Figure SH9: Results of high-resolution melt curve analysis of microbial DNA.

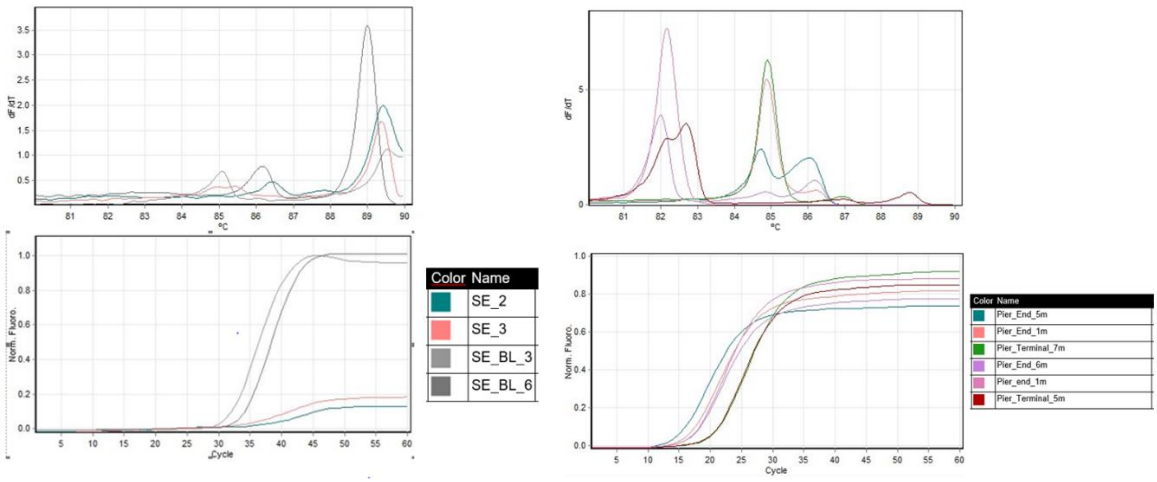

Figure SH10: Results of high-resolution melt curve analysis of microbial DNA.

Corrosion, sediment and seawater samples at Shoreham and Newhaven show comparable melt indicating the same variants of the gene in microbes implicated in MIC (Figure SH9). Corrosion and seawater samples from Southend, where MIC/ALWC has not been identified, show completely different melt curves, indicating different *dsr* gene variants and hence different microbial populations (Figure SH10). This opens up the possibility of using HRM analysis for rapid characterisation of microbial populations at community level, and the inclusion of the presence of corrosion linked microbial populations in corrosion hazard and risk analysis.

Construction

Continuous monitoring of water chemistry parameters and corrosion rate was conducted in Shoreham Port from 2nd to 22nd December 2022. The equipment installed was an Aquaread AP6000 multiparameter probe, with sensors for temperature (T), water electrical conductivity (Cond.), pH, oxidiation-reduction potential (ORP) and chlorophyll. The AP6000 includes an automatic cleaning head which is important for marine applications to prevent obstruction of the senors by biofouling and sediment build-up. The AP6000 was powred by solar panel an linked to a data logger with a Point Orange mobile phone uplink to allow remote download of data via the internet. The AP6000 was programmed to record data every hour. Corrosion rate was monitored using CCube linear polarisation resistance sysem, powered by a solar panel, and enabled for remote dowload of data by an additional mobile phone uplink.The sensors were installed in an existing monitoring site in the port Dredger Berth, adjacent to the floating pontoon used for environmental baseline sampling. The sensors were deployed it to a plastic tube, with pre-drilled holes to allow free flow of water. The tube was installed inside of an access ladder, contained within the U-section of a steel pile. Solar panels and data loggers were secured to the port side railing (Figure SH11).

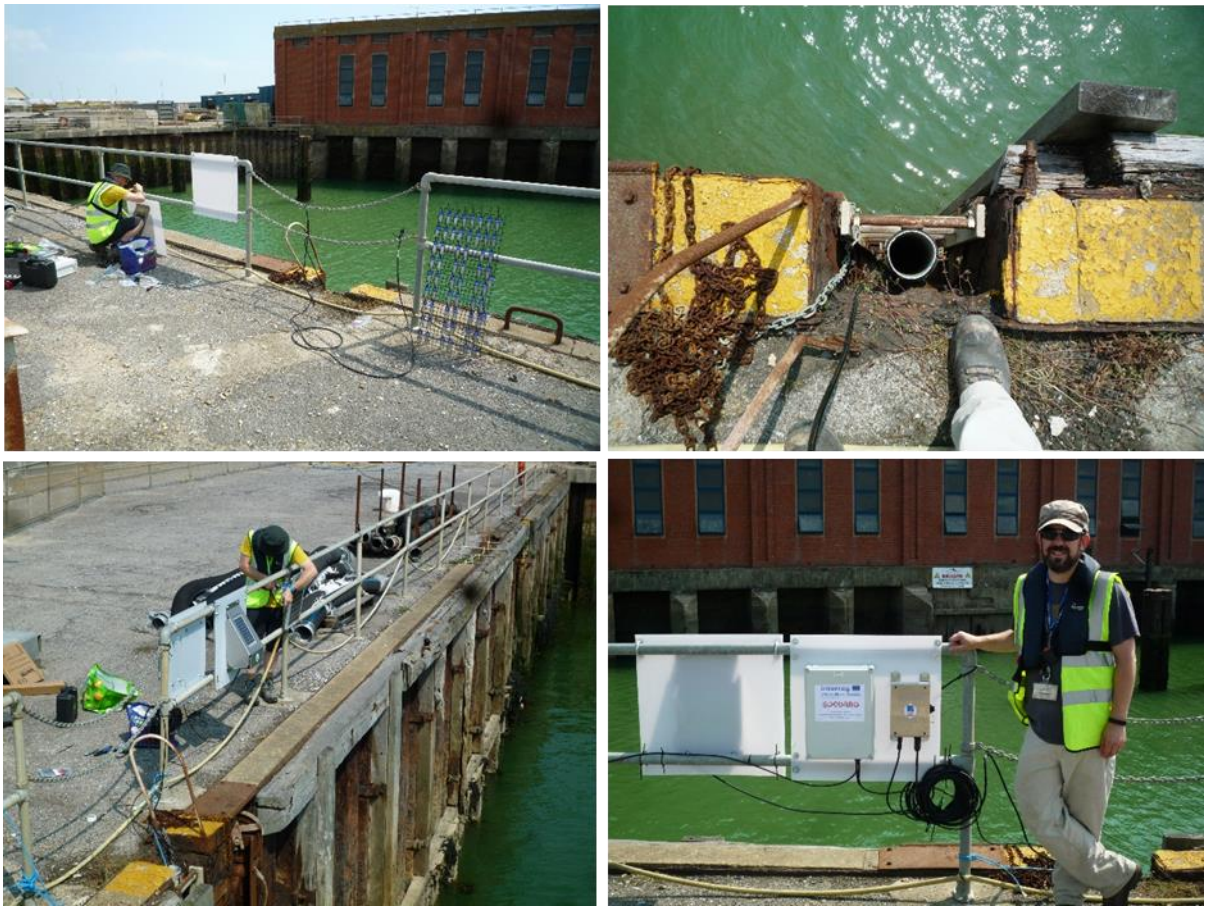

Figure SH11: Installation of the SOCORRO monitoring system at Shoreham harbour.

From mid-September 2022 it became apparent that the CCube systems was recording unrealistically high corrosion rates, and the corrosion monitoring system had a design fault. The rewiring of the system and a successful software upgrade were completed in January 2023, and the system was redeployed at the beginning of February.

Results:

Time series plots from 22 July to 9 September 2022 of all monitored data are shown in Figures SH12 and SH13. The means and ranges of data are shown in Figure SH14. The data are strongly tidlly influenced, and the alternation of spring and neap tides is visible in the depth data (calculated from water pressure) so are frequently bimodal. These cycles influence all other variables. In terms of depth notably on spring low tides the steel piling and the monitoring point can be exposed to atmosphere. Temperature varied between 20-23°C, with a gradual decline from July to September. Dissolved oxygen also varied tidally and correlates strongly with temperature (Figure SH15). Oxidation-reduciton potential (ORP) is relative constant in the water column with a mean aroudn 250-300mV (oxidising environment), but much lower to reducing values occur as outliers. These are typcially at low tide, and may relate to sediment resuspension in shallow water. pH vaires bimodally in relation to the relative input of

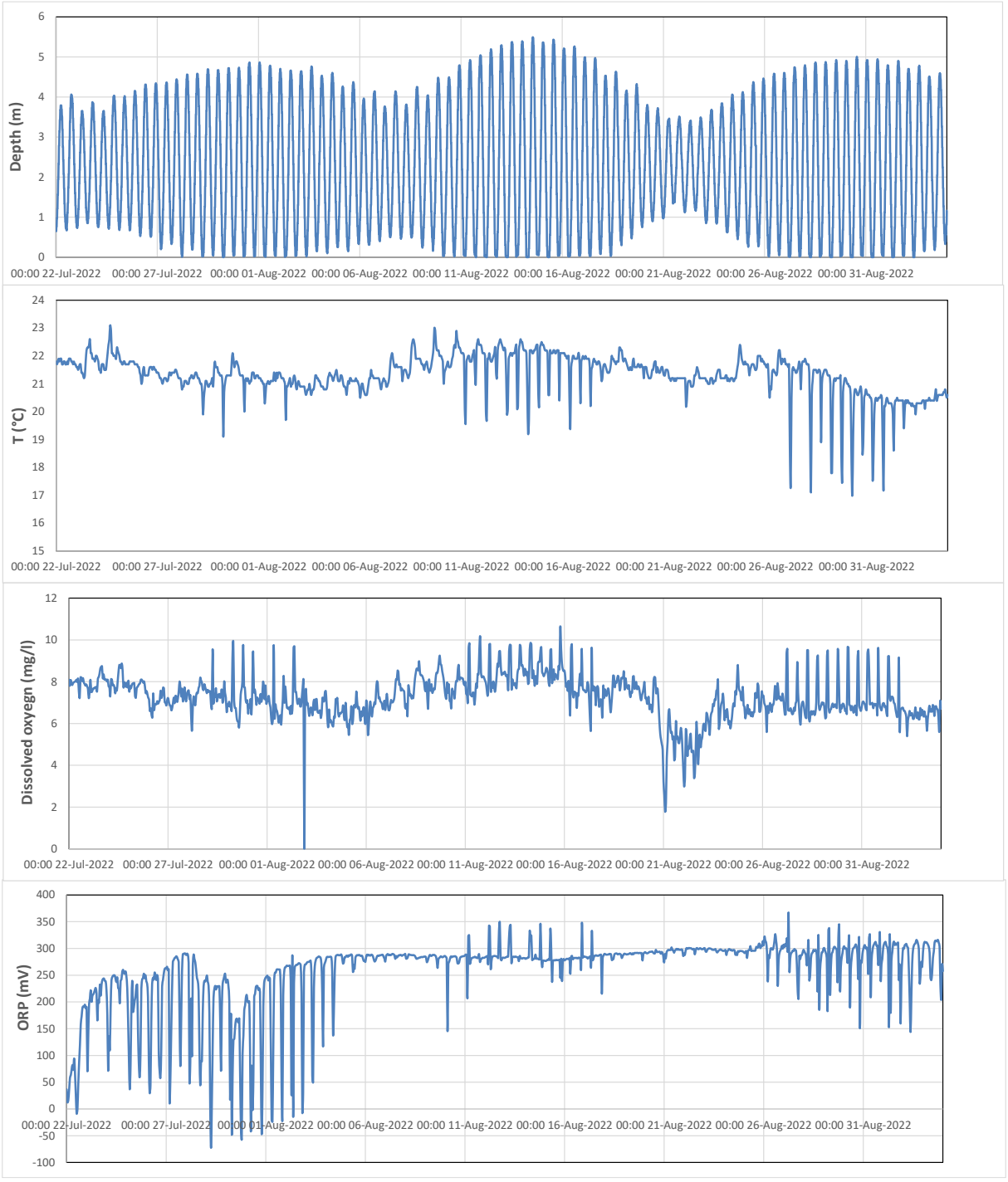

Figure SH12: Time series of water depth, temperature, dissolved oxygen and oxidation-reduction potential (ORP) from Shoreham Dredger Berth.

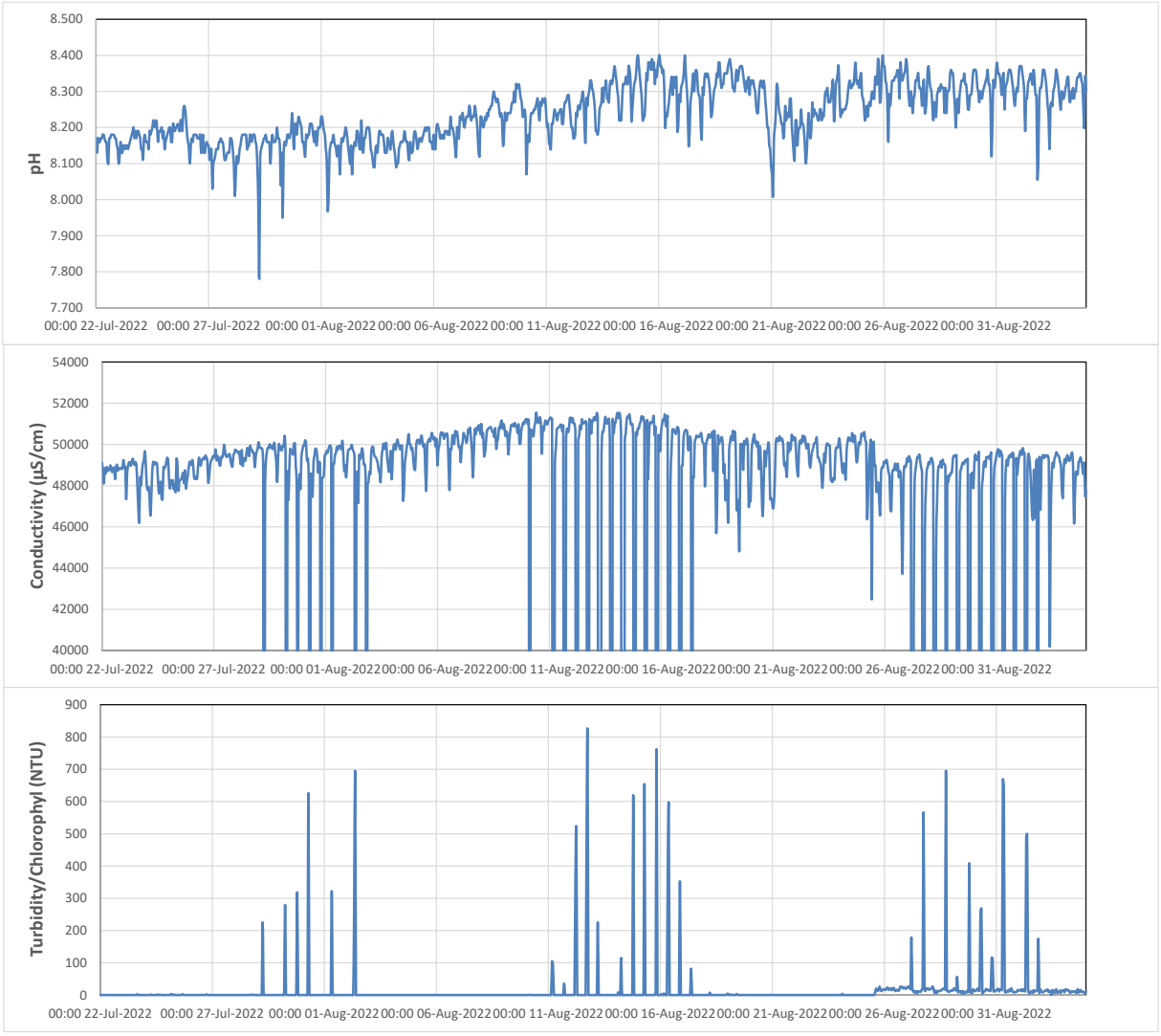

Figure SH12(continued): Time series of pH, conductivity and turbidity/chlorophyll from Shoreham Dredger Berth.

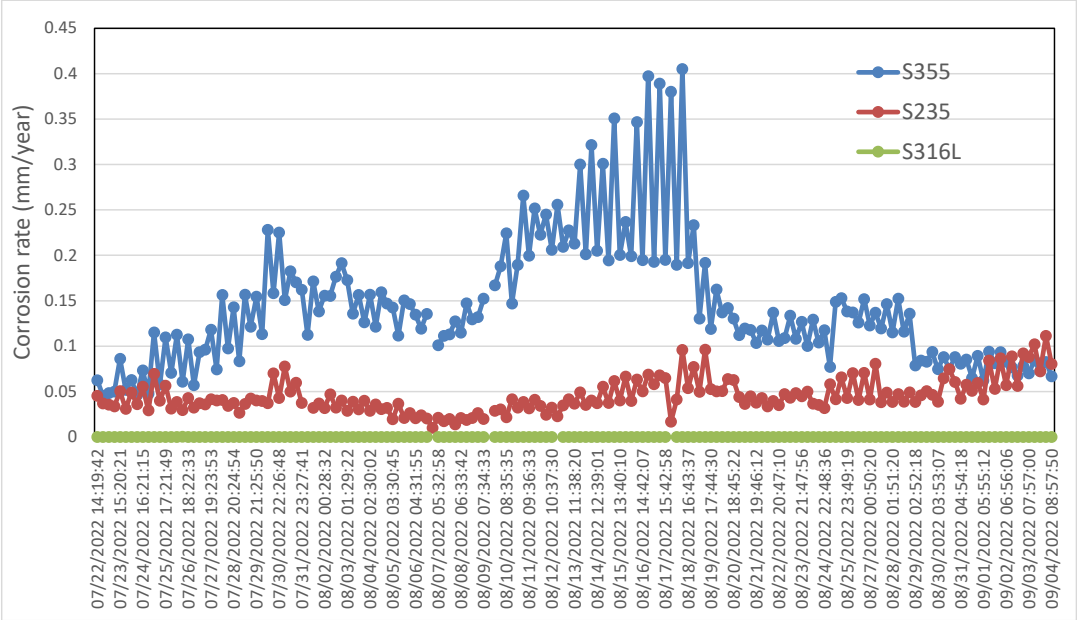

Figure SH13: Time series of corrosion rate in different steel grades from Shoreham Dredger Berth CCube sensor.

marine and freshwater through the tidal cycle in an estuarine environment, as does conductivity. Chlorophyll is typically close to the detection limit of the sensor system, except for isolated peaks presumed to relate to the resuspension of algal material at spring low tides.

The Corrosion rate measured by the CCube instrument at Shoreham varied between 0.01 to 0.1mm/year for S235 steel, from 0.05 to 0.4mm/year for S355 steel, and was typically below 0.01mm/year for S316L (stainless) steel (Fig. SH13). The highest corrosion rates, and the most variation in rate are seen in S355 steel, with an increase in rate related to high temperatures in late August 2022 particularly apparent in the data. Bivariate correlation between corrosion rate and environmental parameters is particularly apparent with dissolved oxygen, temperature and depth (which drives variation in other parameters in a tidal environment) in S355. In S235 significant correlations are with pH and to some extent depth. The difference can be attributed to the overall lower corrosion rate measured in S235. In both S235 and S355 corrosion rate shows negative correlation with T, below 0.1mm/year. These low corrosion rates correlate with the lowest T in each case, and the lowest pH suggesting that corrosion is strongly controlled by pH, under these conditions, with increasing influence from dissolved oxygen at higher concentrations. The highest corrosion rates observed at Shoreham are in S355, during the highest oxygen concentrations and the lowest water levels, but a relative low T. In the context of MIC, if sulphide is generated at the steel surface, it's oxidation on atmospheric exposure will produce highly acid pH and the most rapid corrosion rates, whilst not significantly affecting the pH in the main water column.

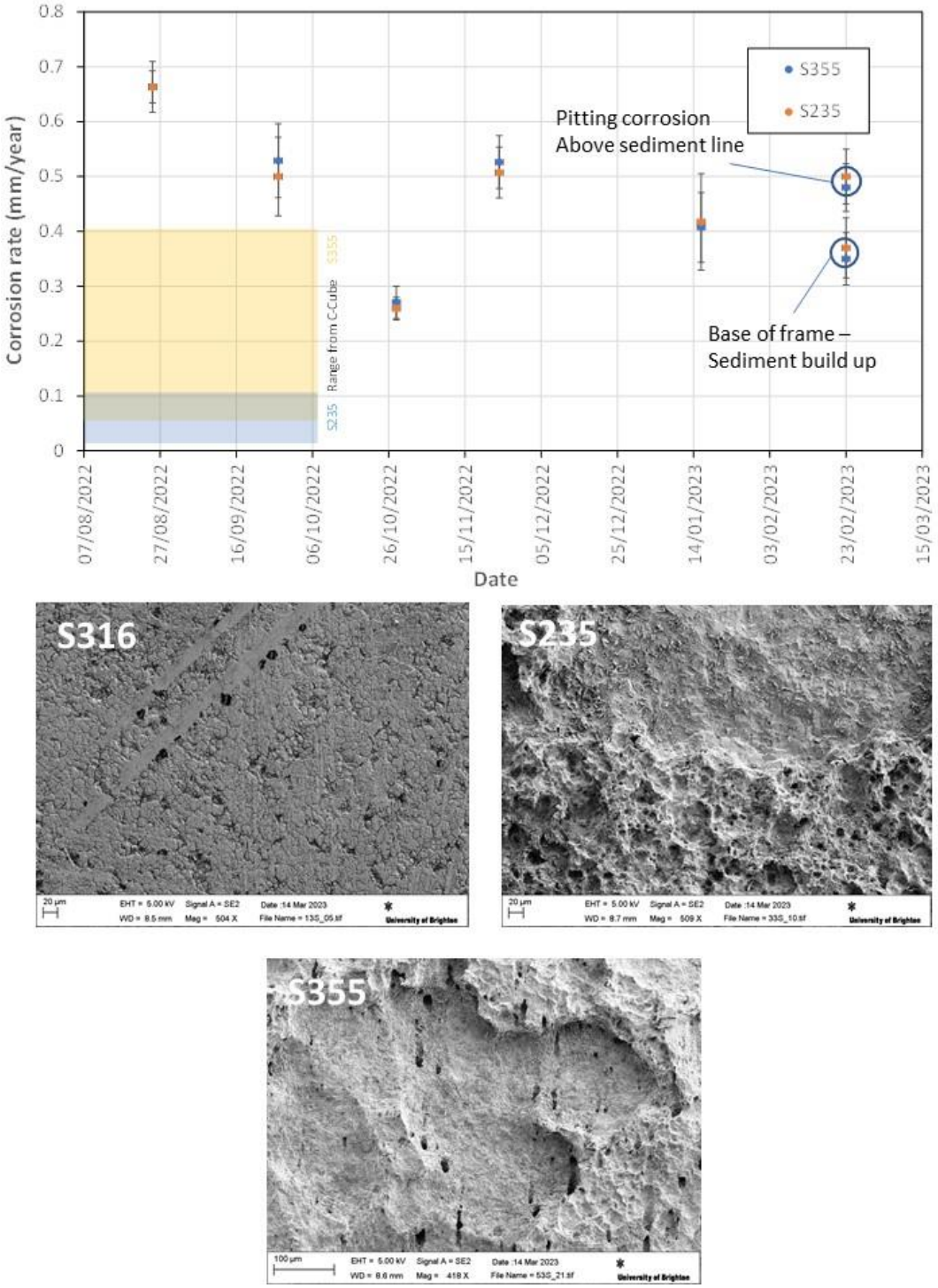

Figure SH14: Top – Corrosion rate data determine from mass loss in steel coupons (S235 and S355). Base – Electron microscope images of steel surface recovered after six months immersion after cleaning. The scale is approximately the same in each image (x500 magnification).

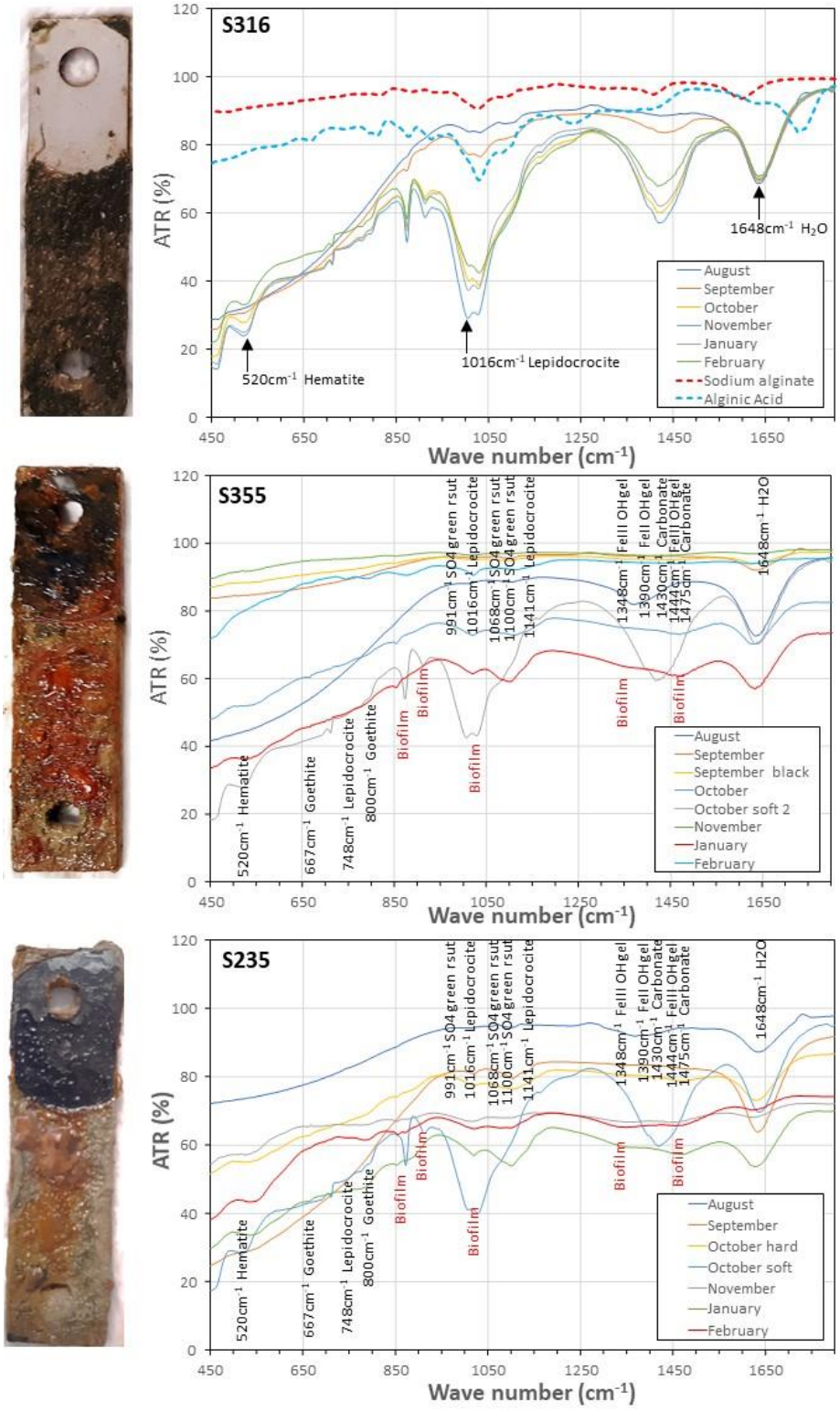

Figure SH15: FTIR spectra of corrosion products and surface deposits from recovered steel coupons.

Steel coupons of each steel grade (S316L; S355; S235) were also installed in the harbour at the same point as the environmental sensors and CCube instrument. These were recovered on a monthly basis and used to determine corrosion rate via measurements of mass loss after cleaning away of corrosion products following ASTM G1-90 (1999). Corrosion products were initially removed with a scaple and saved fro subsequent characterisation. The samples were then cleaned using hydrochloric acid and hexamethylene tetramine. The corrosion rate determined on S316L was always within error of 0mm/year, although SEM examination showed micron scale etch of the steel surface along grain boundaries (Figure SH14). Samples of S355 and S235 showed corrosion rates that were indistinguishable at the resolution of the data and varied from 0.65-0.25mm/year. Both the agreement between the samples, and the corrosion rate are distinct from the CCube measurements. The corrosion rates measured by mass loss are higher in most cases, except for October 2022. This may in part be attributable to the difference in the measurement type. Mass loss is a time integrated measurement, whilst the CCube system measures an instantaneous corrosion rate. There is a general decline in corrosion rate from August to October, that reflects initial formation of corrosion products on the steel surface. Increases from November may be related to biological activity. For the final sample taken (February 2023) there is a lack of agreement between duplicate samples for both S355 and S235. This may relate to position on the deployment frame, as samples at the base of frame show a lower corrosion rate potentially related to sediment build up, whilst from visual inspection those from higher on the frame show development of strong pitting corrosion (SEM images; Figure SH14).

Corrosion products from the recovered coupons were characterised by FTIR in the same way a corrosion samples recovered form steel piles. Samples of S316L showed minimal development of iron oxidation products, as would be expected for stainless steel. However, the development of a surface deposit clearly tracks the colonisation of the steel surface by algae and the development of a polysaccharide biofilm (identified by comparison with laboratory grade sodium alginate and alginic acid; Figure SH 15) by the third month of exposure (October). For samples of S235 and S355 typical crystalline corrosion products are developed (hematite, goethite, lepidocrocite, sulphate green rust, alongside iron hydroxide gels) as seen in the samples taken from the steel pile wall. However, in both cases the October samples also developed red gel like coatings, which are closely comparable to sodium alginate and alginic acid. These track the development of a biofilm over the surface which has been implicated in allowing colonisation of steel by bacteria involved in microbially influenced corrosion (Beech and Sumner, 2004).

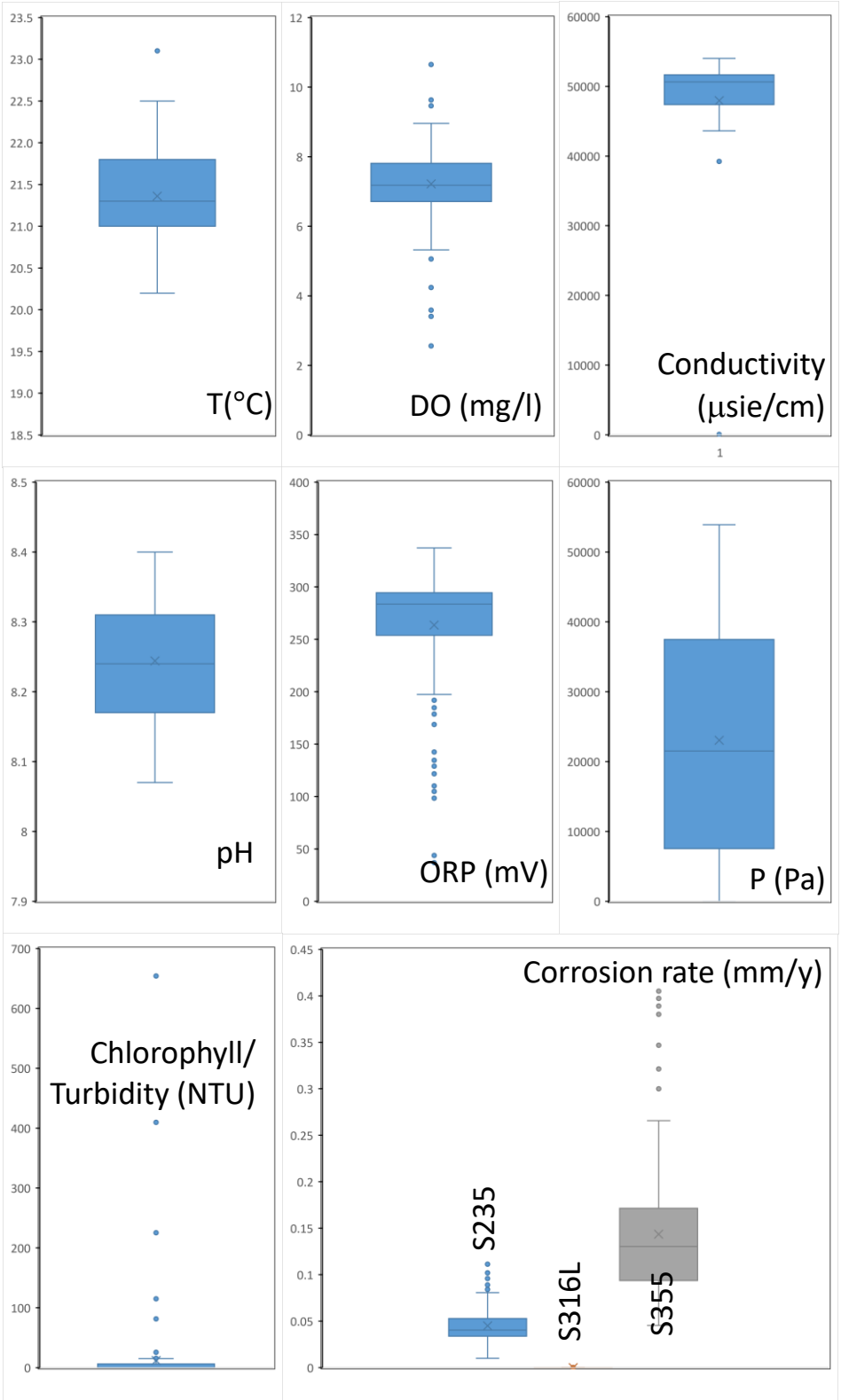

Figure SH16: Box and whisker plots indicating median, upper and lower quartiles and outliers for environmental parameters and corrosion rate.

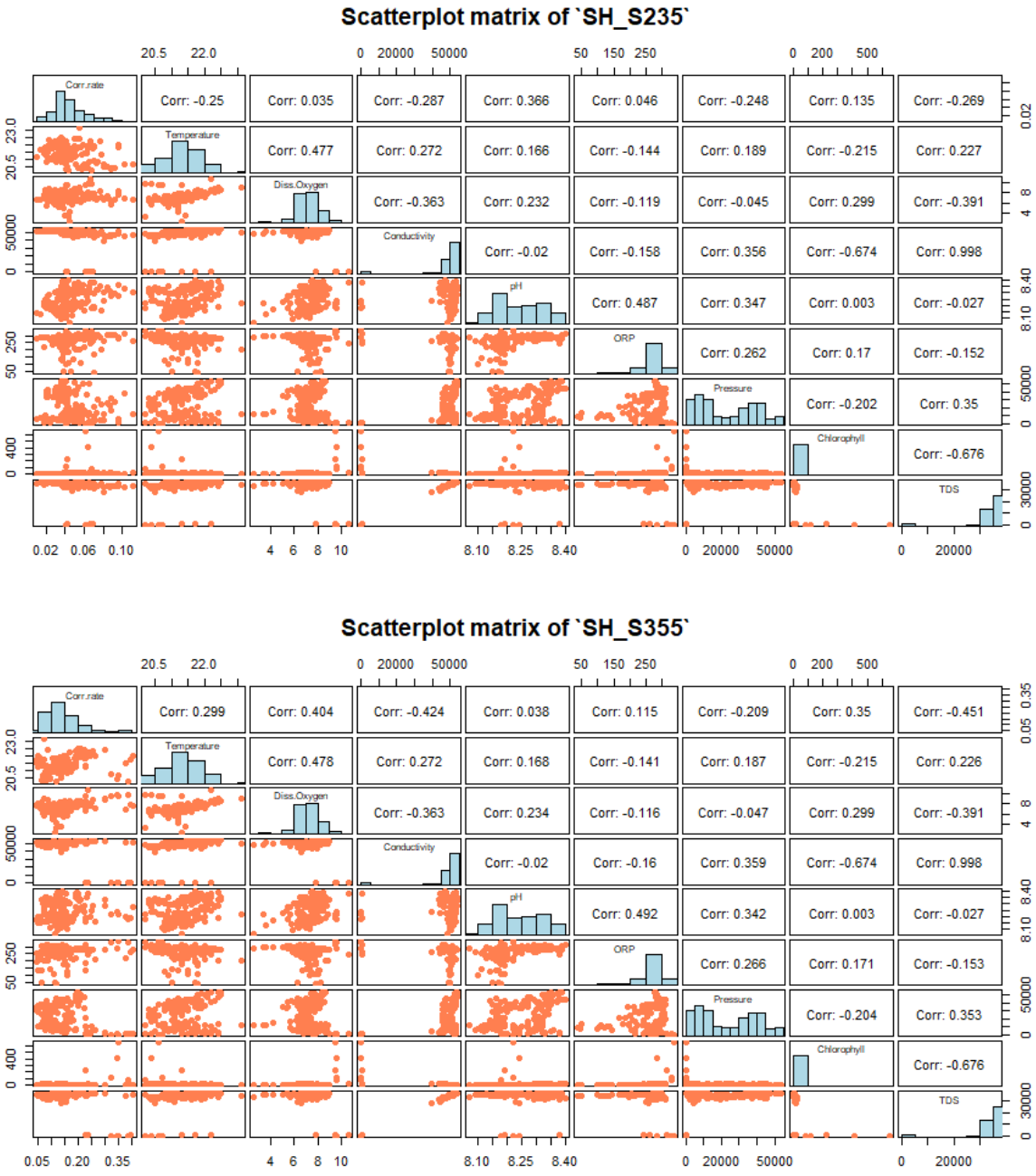

Figure SH17: Bivariate correlation plots and Pearson correlation co-efficients for S235 and S355 steel with environmental parameters.

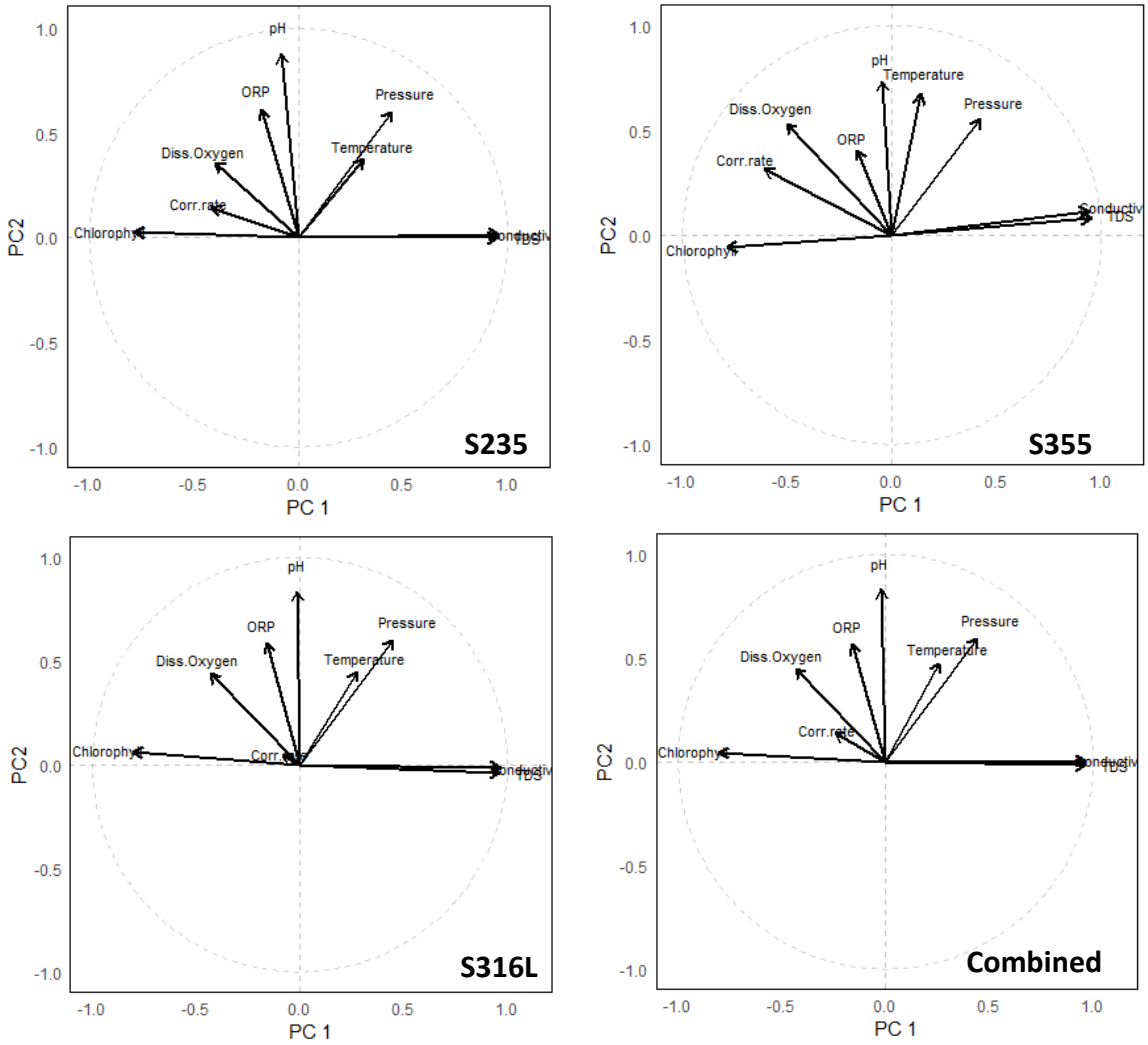

Figure SH18: Results of principal components analysis of corrosion rate and environmental parameters at Shoreham.

The range and mean of corrosion rate measured by the CCube, and for environmental parameters are shown in Figure SH16, and correlations between variables in Figure SH17. The data were also analysed using multivariate statistics via principal components analysis. The weightings of individual variables within the first 2 principle components at shown in Figure SH18. In all cases the majority of variation in the data is accounted for by conductivity, which varies with the relative fresh and marine water contributions in the tidal cycle. In both S235 and S355 PC1 (33.7% of variation) is dominated by variation in conductivity and chlorophyll, and PC2 (is dominated by pH, temperature and dissolved oxygen. The variation in corrosion rate follows the same trends as dissolved oxygen. temperature and pressure (water depth) are positively weighted in both components. When the principal components are plotted against each other for each measurement point (Figure SH19) it is clear the highest corrosion rates

(high PC2) correlate with high temperature and pH when fully immersed (pressure is also high), but that PC retains positive weightings (high corrosion rate, dissolved oxygen) when PC1 is negative, corresponding to periods of very low water or atmospheric exposure.

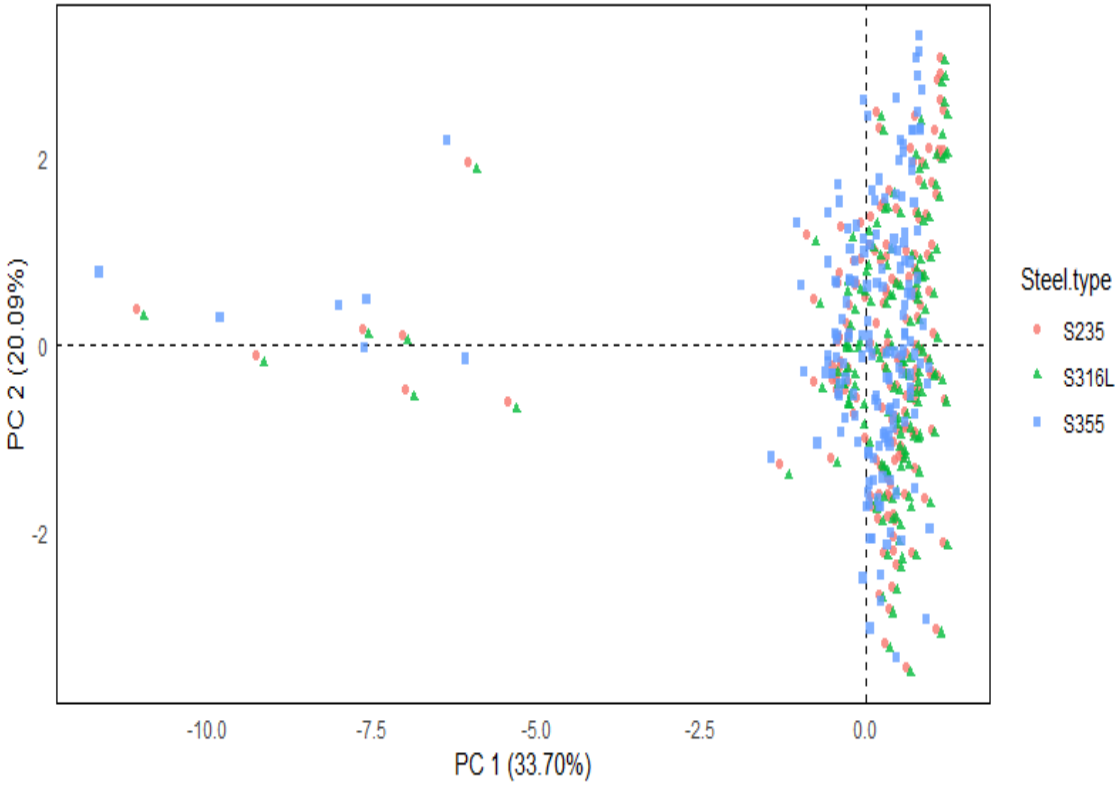

Figure SH19: Results of principle components analysis for each measurement time.

Overall the statistical analysis shows that there are two regimes driving high corrosion rate. When the steel is fully immersed then corrosion rate correlates positively with temperature and dissolved oxygen. At low tide the exposure to atmospheric oxygen drives accelerated corrosion rate independently of temperature. These can be related to corrosion mechanism whereby temperature increase reaction rates during immersion, but corrosion reactions consume oxygen and are thus accelerated further during very low water and atmospheric exposure.

Figure SH20: Out put from the SOCORRO corrosion risk application. (A) Display of monitoring data. (B) Predicted corrosion risk. (C) Predicted corrosion risk averaged over a 10 hour period. (D) Cumulative corrosion risk. Thresholds of critical corrosion risk are arbitrarily set at 0.2 and the cumuative corrosion risk at 200 to demonstrate the visualisation capabilities.

Analysis of the monitoring data rom Shoreham using he SOCORRO application is shown in Figure SH20. The forward prediction was made using the the 'Seawater, Field Trained' algorithm, which is based on the July to September monitoring period at Shoreham. The results strongly highlight the influence of the high temperature period in August 2022, where increased corrosion risk can be seen, alongside an acceleration in the rate of accumualted corrosion risk. Individual short term (hours) periods of corrosion risk are predicted forward of the training period at spring low tides whent the steel work is exposed to atmosphere. This is in agreement with results of multivariate statisitical analysis of the data, and is result of enhanced oxygen concentrations on exposure, and potentially the oxidation of bactierially produced sulphides during these periods.

Plans for further use?

The Shoreham monitoring site has been maintained since July 2022. The CCube sensor stopped providing reliable data from mid-September 2022, and was removed for repair in January 2023. The CCube sensor has now been reinstalled (February 2023) and with the support of Shoreham Port Authority will be maintained for at least another 6 months to allow collection of a data set that will allow full interpretation of the changes in corrosion rate with environmental parameters through multiple seasons, and demonstration of the SOCORRO system over an extended period.

References.

ASTM G1-90 (1999) Standard practice for preparing, cleaning and evaluating corrosion test specimens.

I.B. Beech, J.A. Sunner, K. Hiraoka, Microbe-surface interactions in biofouling and biocorrosion processes, International microbiology, 8 (2005) 157-168.

I.B. Beech, J. Sunner, Biocorrosion: towards understanding interactions between biofilms and metals, Current opinion in Biotechnology, 15 (2004) 181-186.

M.J. Borda, D.R. Strongin, M.A. Schoonen, A vibrational spectroscopic study of the oxidation of pyrite by molecular oxygen, Geochimica et Cosmochimica Acta, 68 (2004) 1807-1813.

I. Chernyshova, An in situ FTIR study of galena and pyrite oxidation in aqueous solution, Journal of Electroanalytical Chemistry, 558 (2003) 83-98.

S. Peulon, L. Legrand, H. Antony, A. Chaussé, Electrochemical deposition of thin films of green rusts 1 and 2 on inert gold substrate, Electrochemistry communications, 5 (2003) 208-213.

V. Rouchon, H. Badet, O. Belhadj, O. Bonnerot, B. Lavédrine, J.G. Michard, S. Miska, Raman and FTIR spectroscopy applied to the conservation report of paleontological collections: identification of Raman and FTIR signatures of several iron sulfate species such as ferrinatrite and sideronatrite, Journal of Raman Spectroscopy, 43 (2012) 1265-1274

B. Rousell, Hall's Aggregate Wharf Dive Survey 2011, in, Shoreham Port Engineering Department, 2012

RRUFF database. http://rruff.info/about/about_general.php

R. Sachan, A.K. Singh, Comparison of microbial influenced corrosion in presence of iron oxidizing bacteria (strains DASEWM1 and DASEWM2), Construction and Building Materials, 256 (2020) 119438

M. Shahabi-Navid, Y. Cao, J.-E. Svensson, A. Allanore, N. Birbilis, L.-G. Johansson, M. Esmaily, On the early stages of localised atmospheric corrosion of magnesium–aluminium alloys, Scientific Reports, 10 (2020) 1-16.

C.R. Usher, K.W. Paul, J. Narayansamy, J.D. Kubicki, D.L. Sparks, M.A. Schoonen, D.R. Strongin, Mechanistic aspects of pyrite oxidation in an oxidizing gaseous environment: An in situ HATR− IR isotope study, Environmental science & technology, 39 (2005) 7576-7584

V. Zinkevich, I. Bogdarina, H. Kang, M. Hill, R. Tapper, I. Beech, Characterisation of exopolymers produced by different isolates of marine sulphate-reducing bacteria, International Biodeterioration & Biodegradation, 37 (1996) 163-172